

HTMNet: A Hybrid Network with Transformer-Mamba Bottleneck Multimodal Fusion for Transparent and Reflective Objects Depth Completion

Guanghu Xie, Yonglong Zhang, Zhiduo Jiang, Yang Liu[†], Zongwu Xie, Baoshi Cao, Hong Liu

Abstract—Transparent and reflective objects pose significant challenges for depth sensors, resulting in incomplete depth information that adversely affects downstream robotic perception and manipulation tasks. To address this issue, we propose HTMNet, a novel hybrid model integrating Transformer, CNN, and Mamba architectures. The encoder is constructed based on a dual-branch Transformer-CNN framework, while the multi-scale fusion module leverages a Transformer-Mamba architecture, which also serves as the foundation for the decoder design. We introduce a novel multimodal fusion module grounded in self-attention mechanisms and state space models, marking the first application of the Mamba architecture in the field of transparent object depth completion and revealing its promising potential. Additionally, we design an innovative multi-scale fusion module for the decoder that combines channel attention, spatial attention, and multi-scale feature extraction techniques to effectively integrate multi-scale features through a down-fusion strategy. Extensive evaluations on multiple public datasets demonstrate that our model achieves state-of-the-art(SOTA) performance, validating the effectiveness of our approach.

Index Terms—Depth Inpainting, Transparent and Reflective Object, State Space Models,

I. INTRODUCTION

The acquisition of accurate depth information for transparent and reflective objects remains a significant challenge in the field of computer vision [1]. These objects exhibit unique optical characteristics due to their transparency and reflectivity, which conflict with common depth imaging assumptions [2] [3]. This conflict renders traditional depth imaging methods ineffective for such objects, making it difficult to obtain their 3D information [4].

3D geometric data, such as point clouds and depth maps, play a crucial role in vision-based perception and detection tasks. Existing depth sensors, including LiDAR and depth cameras, primarily rely on infrared light to acquire geometric information. However, infrared light penetrates transparent objects and undergoes specular

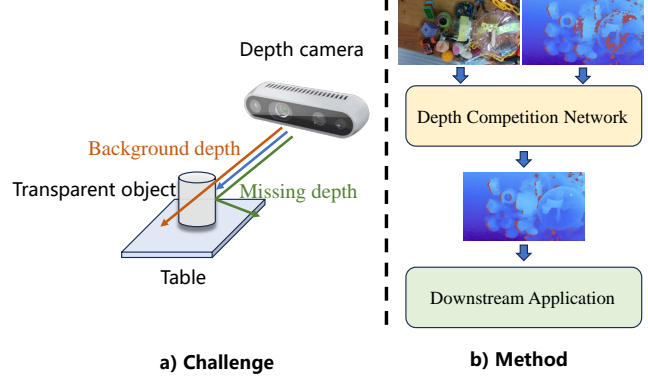


Fig. 1. a) illustrates two typical types of errors encountered when capturing the depth of transparent objects using depth cameras: one is missing depth information, and the other is the erroneous acquisition of background depth; b) depicts the general pipeline in which a depth completion model is used to recover the depth of transparent objects, which is subsequently fed into downstream tasks.

reflection on reflective surfaces, making depth estimation challenging and introducing substantial noise [2] [5]. As illustrated in Fig.1 a), the introduction of background depth and missing depth are two typical challenges that lead to inaccurate depth measurements for transparent and reflective objects.

The causes of depth loss are multifaceted, involving both optical and geometric factors. Transparent and reflective objects attenuate light signals, while object occlusion and sensor disparity lead to depth information loss [6]. Even after calibration, misalignment between RGB and depth cameras results in optical parallax and missing depth map blocks [7] [8].

The difficulties in recovering the 3D information of transparent and reflective objects mainly stem from two aspects. First, the complex optical properties of these objects pose challenges for cameras when acquiring RGBD images [3] [9] [10]. Transparent objects suffer from feature masking due to background color transmission and refractive distortion, while reflective objects exhibit issues such as specular highlights and environment mapping [4]-[9]. These issues disrupt traditional depth information acquisition methods like structured light and stereo vision. Additionally, multipath effects and refractive errors introduce noise and artifacts, leading to edge blurring

[†] Corresponding author: Yang Liu (liuyanghit@hit.edu.cn).

*This work was supported by the Natural Science Foundation of Heilongjiang Province for Excellent Young Scholars (Grant No. YQ2024E018) and the Youth Talent Support Program of the China (Grant No. 2022-JCJQ-QT-061).

All authors are with the State Key Laboratory of Robotics and Systems, Harbin Institute of Technology, Harbin 150001, Heilongjiang, China

and topological errors in depth reconstruction.

Numerous research efforts have been dedicated to acquiring depth information for transparent and reflective objects, including methodologies such as monocular depth estimation and depth completion based on incomplete depth data. Monocular RGB image depth estimation is inherently ill-posed due to the lack of geometric constraints [11] [12]. To address this, sparse depth priors are introduced, transforming the task into a depth inpainting process from sparse to dense [3]. This approach leverages physically meaningful depth signals to guide the model, generating dense depth maps that conform to the real scene structure. This method enhances the stability and accuracy of depth reconstruction by integrating multimodal information. Depth completion aims to recover the missing depth values of such objects through a learning-based approach, thereby enabling accurate perception for downstream tasks, as shown in Fig.1 b). Fig.2 presents an application example of depth completion, where the completed depth of transparent and specular objects is used for multi-finger dexterous grasp detection. This facilitates a higher grasp success rate.

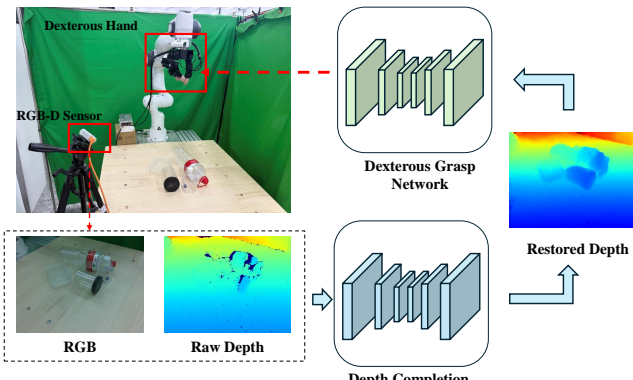


Fig. 2. Depth completion plays a crucial role in dexterous grasping applications. When grasping transparent or specular objects, depth completion is first performed to obtain relatively complete depth information. The completed depth maps are then fed into a dexterous grasping network for grasp detection. This process effectively addresses the failure of grasp detection caused by missing depth information in transparent or specular objects.

Models based on Transformer and CNN have been widely applied in the field of transparent object depth completion. To the best of our knowledge, however, there are currently no reported applications of the Mamba architecture in this domain. To address this long-standing gap, we conduct our research to explore the potential of the Mamba architecture in this context, aiming to open new research avenues for the community.

The main contributions of our work are summarized as follows:

- **We propose a novel dual-branch hybrid architecture integrating Transformer, CNN, and**

Mamba. In this design, the Transformer branch extracts features from RGB-D images, the CNN branch extracts features from depth maps, and a bottleneck multimodal fusion is performed based on attention mechanisms and state-space models. This represents a new hybrid architecture tailored for depth completion of transparent objects.

- **We develop a Transformer-Mamba-based bottleneck multimodal fusion module.** By leveraging self-attention mechanisms and state-space modeling, the module effectively fuses multimodal features, fully exploiting the complementary advantages of different paradigms. To the best of our knowledge, this is the first application of state-space models to the field of transparent object depth completion.
- **We propose a novel multi-scale fusion module.** It integrates spatial attention, channel attention, and multi-scale feature fusion mechanisms into a unified down-fusion structure for the decoder.
- We conduct extensive evaluations on multiple public datasets for transparent object depth completion, achieving **state-of-the-art(SOTA)** performance.

II. RELATED WORKS

A. Depth Completion for Single View Transparent Objects

Depth completion, as a fundamental task in computer vision, typically uses raw depth and RGB images to recover missing depth values in depth maps [13] [14] [15] [16]. Due to the convenience of single-view acquisition and rapid data capture, depth completion for transparent and reflective objects under monocular settings has become a research hotspot. Before end-to-end models were applied to depth completion, two approaches were adopted for transparent object depth completion. The first relies on external assumptions, such as specialized sensing devices [17] and predefined backgrounds [18]. However, these methods are unsuitable for random environments due to their dependency on external assumptions. To overcome these limitations, a second approach using global optimization algorithms emerged [19]. Studies in [20], [21] utilized sensor-captured RGB-D images as input for depth completion, eliminating the need for external assumptions. However, they rely on surface normal and edge predictions, a limitation later addressed by end-to-end models. In [22], a generative adversarial network (GAN) was employed to generate depth maps for transparent object reconstruction. In [23], a multi-scale depth network was proposed, combining RGB and depth images as input. Although both ToDE-Trans [24] and swinDRNet [5] adopt Swin Transformers, they differ significantly in architecture. Specifically, swinDRNet is a dual-stream fusion network that integrates raw depth information with predicted depth through confidence maps, while ToDE-Trans follows a classical

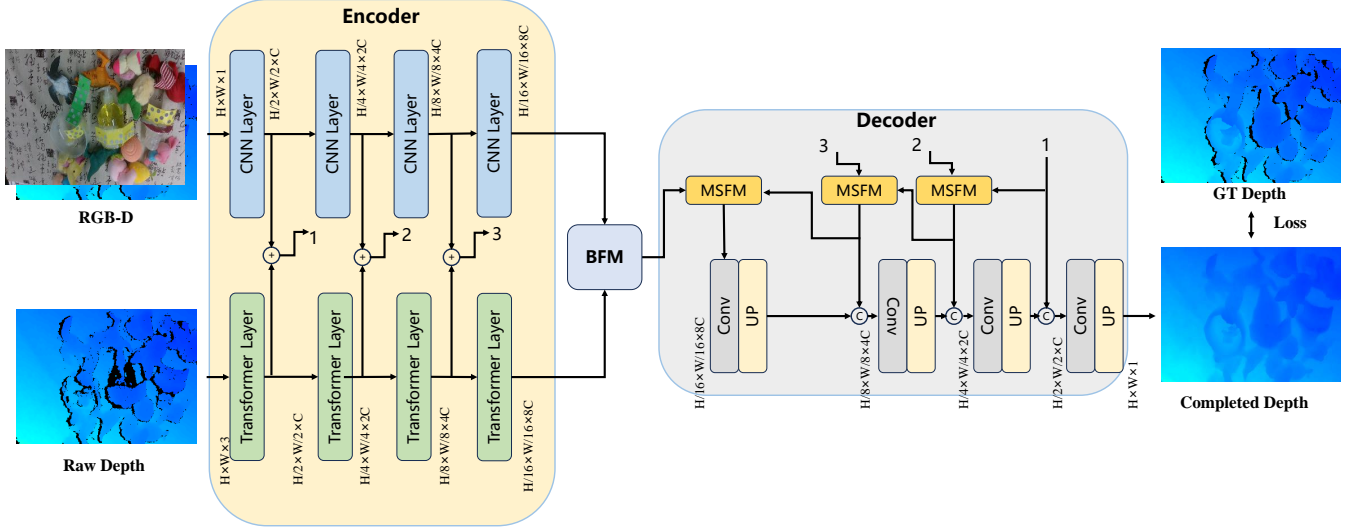


Fig. 3. HTMNet Architecture. Our method consists of a dual-branch encoder, a bottleneck fusion module, and a decoder. The Transformer-based backbone extracts RGB-D features, while the CNN-based backbone extracts depth features. The bottleneck fusion module performs multimodal fusion at the network bottleneck, and the decoder is composed of a multi-scale fusion module, convolutional layers, and upsampling operations.

encoder-decoder structure. In [25], a decoder with multiple cascaded "refinement modules" was designed. In [26], to enable cross-level feature fusion and better leverage low-level depth features, researchers introduced a skip-connected fusion branch within a U-Net framework.

B. CNN-Transformer Hybrid Architecture for Vision Tasks

In visual recognition tasks, Vision Transformer (ViT) models have achieved remarkable success due to their superior performance [27]. However, the multi-head self-attention (MHA) mechanism not only incurs high computational costs but also struggles to capture inductive biases for local relationships. To address this issue, numerous studies have explored novel approaches to integrate convolutional mechanisms with self-attention. For instance, Li et al. [28] introduced MSA at the front end of the model while employing CNNs at the backend, a design that contrasts sharply with the method in [29], where CNNs first extract local features and MSA then learns long-range dependencies. In certain specialized tasks, the parallel use of CNNs and Transformers has gradually become a common strategy. Taking [30] as an example, researchers typically extract features separately through CNN and Transformer branches, followed by feature fusion at later stages. Additionally, in [31] and [32], convolutional and attention mechanisms are jointly utilized to construct modules, which are iteratively applied throughout the network. Despite the diversity of these fusion strategies, their core objective remains consistent: enabling models to simultaneously learn global and local information.

C. Vision Mamba

Since its emergence, Mamba has garnered significant attention in the research community, with numerous efforts devoted to developing vision models based on the Mamba architecture [33] [34]. VMamba [35] is a vision-oriented model built upon the Mamba architecture, specifically designed for image processing tasks. It introduces a novel 2D Selective Scan mechanism that effectively expands the receptive field and aligns well with the structural characteristics and requirements of visual perception tasks. MambaVision [36] effectively integrates CNN and the Mamba architecture, enabling it to capture both long-range and short-range dependencies. EfficientVMamba [37] introduces a skip-sampling mechanism and a atrous-based selective scanning approach. U-Mamba [34] integrates state space models with convolutional neural networks (CNNs) and has been successfully applied to the field of medical image segmentation. VM-UNet [38] and Mamba-UNet [39] construct complete encoder-decoder architectures based on state space models (SSMs).

III. METHOD

Our proposed model mainly consists of three components: a dual-branch Transformer-CNN encoder, a bottleneck fusion module based on the self-attention mechanism and state-space model, and a decoder based on a multi-scale fusion module. The following sections will provide a detailed introduction to each component.

A. Dual-branch Transformer-CNN encoder

Transformer tend to capture global features, while CNNs are more adept at capturing local features. To

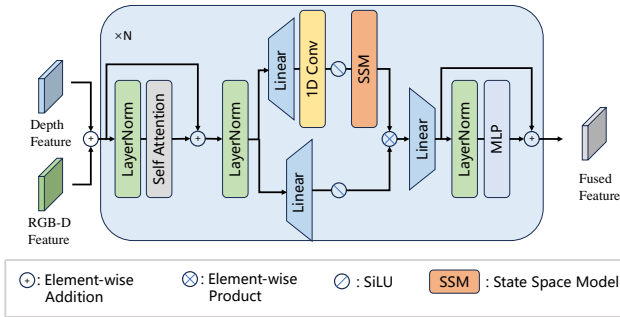


Fig. 4. Bottleneck fusion module(BFM): Composed of Transformer and Mamba modules, multimodal features are pixel-wise summed and then sequentially processed through a self-attention block, a Mamba block, and an MLP to output enhanced fused features.

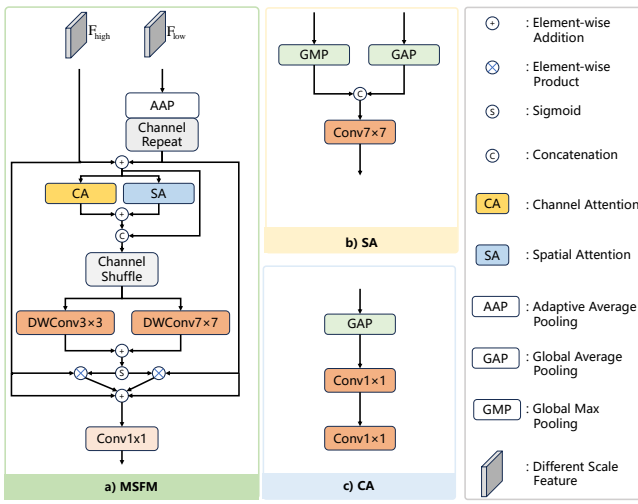


Fig. 5. Multi-scale fusion module(MSFM): Constructed based on spatial attention, channel attention, and multi-scale feature extraction mechanisms, it fuses multi-scale features from the encoder for the decoder.

fully leverage the strengths of both, our proposed encoder consists of two branches: a Transformer branch and a CNN branch. The Transformer branch is utilized to extract RGB-D image features, while the CNN branch is employed to extract depth image features, similar to the approach in [40].

We adopt the Swin Transformer [41] as the backbone of the Transformer branch and ResNet [42] as the backbone of the CNN branch to extract feature information from the two different modalities, respectively. Subsequently, we perform simple feature addition to fuse the shallow dual-modal features, while the deep features are fused using a bottleneck fusion module based on the self-attention mechanism and state-space model.

B. Bottleneck fusion module

The hybridization of Transformers and SSMs has been proven beneficial for long-sequence processing, and re-

cent studies in the medical field [43] have also demonstrated their potential in the visual domain. To explore their application potential in multimodal feature fusion and depth completion of transparent objects, inspired by [43], we designed a multimodal feature fusion module based on the self-attention mechanism and state-space model. This module is utilized at the bottleneck of the dual-branch backbone to fuse deep multimodal features. Fusion at the bottleneck, compared to layer-by-layer fusion, reduces computational costs while achieving higher performance, as validated in the supplementary experiments. The following sections will provide a detailed introduction to this fusion module.

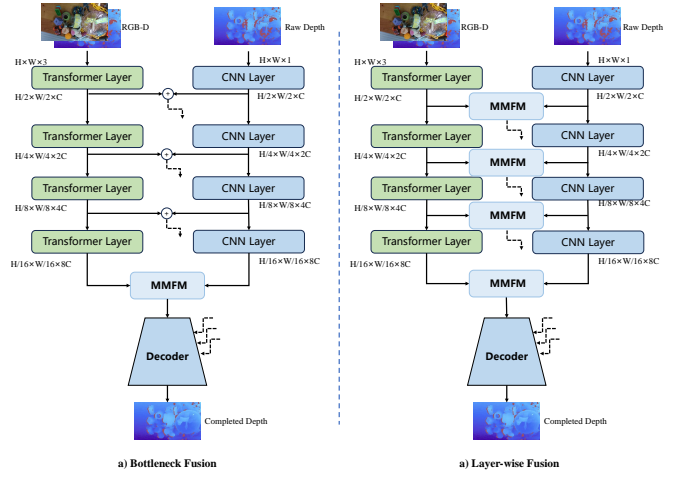


Fig. 6. Comparison of Different Fusion Methods: a) Fusion Module at Deep Bottleneck; b) Layer-wise Fusion Modules. MMFM Represents Multi-Modal Fusion Module.

Space-state Models(SSMs). We first introduce the preliminary knowledge of SSMs. SSMs utilize a conventional continuous system that transforms a one-dimensional input function or sequence, represented as $x(t) \in \mathbb{R}^N$, through intermediate implicit states $h(t) \in \mathbb{R}^N$, to produce an output $y(t) \in \mathbb{R}^N$. This process can be described by the following equation:

$$\begin{aligned} h'(t) &= \mathbf{A}h(t) + \mathbf{B}x(t) \\ y(t) &= \mathbf{C}h(t) \end{aligned} \quad (1)$$

Where $\mathbf{A} \in \mathbb{R}^{N \times N}$ is the state transition matrix, while $\mathbf{B} \in \mathbb{R}^N$ and $\mathbf{C} \in \mathbb{R}^N$ are the input and output projection parameters, respectively.

Structured State Space Sequence Models(S4) and Mamba discretize this process to better suit deep learning applications. An alternative approach is presented in the following equation:

$$\begin{aligned} \bar{\mathbf{A}} &= \exp(\Delta \mathbf{A}) \\ \bar{\mathbf{B}} &= (\Delta \mathbf{A})^{-1}(\exp(\Delta \mathbf{A}) - I) \cdot \Delta \mathbf{B} \\ h_t &= \bar{\mathbf{A}}h_{t-1} + \bar{\mathbf{B}}x_t \\ y_t &= \mathbf{C}h_t \end{aligned} \quad (2)$$

Where Δ is the discretization interval. With the above preliminary knowledge, we next introduce the structure of our fusion module.

First, we perform element-wise addition of the RGB-D modality feature $X_r \in \mathbb{R}^{B \times C \times H \times W}$ and depth modality feature $X_d \in \mathbb{R}^{B \times C \times H \times W}$ to obtain the initial fused features:

$$X_f = X_r + X_d \quad (3)$$

Then, the initial fused features are passed through a multi-head self-attention mechanism(MHA) to extract global features:

$$X_f = \text{LN}(X_f + \text{MHA}(X_f)) \quad (4)$$

Next, the fused feature $X_f \in \mathbb{R}^{B \times L \times C}$ is further enhanced through the Mamba block, which consists of two parallel branches. One branch expands the features to $(B, 2L, C)$ through a linear expansion layer, followed by a SiLU activation function. The other branch first expands the features through a linear layer, and then sequentially applies a 1D convolution, a SiLU activation function, and an SSM layer. Finally, the outputs of the two branches are fused using the Hadamard product:

$$X_f = W_{\text{down}}(\text{SSM}(\delta(\text{Conv}(W_{\text{up}}X_f)))) \odot \delta(W_{\text{up}}X_f) \quad (5)$$

where $\text{SSM}(\cdot)$ represents the state-space model. $W_{\text{up}} \in \mathbb{R}^{C \times EC}$ and $W_{\text{down}} \in \mathbb{R}^{EC \times C}$ are linear layers, where E is expansion ratio. $\text{Conv}(\cdot)$ denotes 1D convolution operation, $\delta(\cdot)$ is SiLU activation function, and \odot represents element-wise multiplication.

Next, the fused features are fed into the MLP block:

$$X_f = \text{LN}(X_f + \text{MLP}(X_f)) \quad (6)$$

C. Multi-Scale Fusion Decoder

Our decoder structure is inspired by [40]. We integrate features of different scales through a multi-scale fusion module, as illustrated in Fig.3. First, we perform down-sampling and channel replication on the shallow features to ensure that the features from different scales have the same shape. Then, we compute the weights of features at different scales based on the spatial attention mechanism and the channel attention mechanism:

$$\begin{aligned} \hat{F}_{i-1} &= \text{CR}(\text{AAP}(F_{i-1})) \\ X &= F_i + \hat{F}_{i-1} \\ \text{SA}(X) &= C_{7 \times 7}([\text{GMP}(X), \text{GAP}(X)]) \\ \text{CA}(X) &= C_{1 \times 1}(\text{C}_{1 \times 1}(\text{GAP}(X))) \end{aligned} \quad (7)$$

where F_i denotes the feature map of the i -th layer and $i \in \{1, 2, 3\}$. $\text{CR}(\cdot)$ represents the channel repetition operation, and $\text{AAP}(\cdot)$ denotes adaptive average pooling. $\text{SA}(\cdot)$ and $\text{CA}(\cdot)$ denote spatial attention and channel attention, respectively. $C_{1 \times 1}$ and $C_{7 \times 7}$ indicate convolution operations with kernel sizes of 1×1 and 7×7 , respectively.

$\text{GAP}(\cdot)$ and $\text{GMP}(\cdot)$ denote global average pooling and global max pooling, respectively.

To fully integrate the weights from different attention mechanisms, we perform channel shuffling to ensure thorough interleaving of the weights. Subsequently, the final weights are obtained through multi-scale DWConv and a Sigmoid activation function.

$$\begin{aligned} X_w &= \text{CS}([\text{SA}(X) + \text{CA}(X), X]) \\ W &= \sigma(\text{DWConv}_{3 \times 3}(X_w) + \text{DWConv}_{7 \times 7}(X_w)) \quad (8) \\ X_{\text{out}} &= C_{1 \times 1}(W \otimes F_i) + C_{1 \times 1}((1 - W) \otimes \hat{F}_{i-1}) \end{aligned}$$

Where \otimes is element-wise product. DWConv represents depth-wise convolution. σ is the sigmoid function. CS means channel shuffle operation.

D. Loss function

Similar to previous works [23] [40], our loss function mainly consists of two parts. One is the MSE loss between the predicted depth values and the ground truth, which serves as the primary loss. Additionally, we employ a normal-based auxiliary smoothing loss function, as shown in the following equation:

$$\begin{aligned} L_{\text{mse}} &= \|D - D^*\|^2 \\ L_{\text{smooth}} &= 1 - \cos(V^* \times V) \\ L_d &= L_{\text{mse}} + \alpha L_{\text{smooth}} \end{aligned} \quad (9)$$

where D and D^* denote the predicted and ground truth depth maps, respectively. V and V^* represent the predicted and ground truth normal vectors. α is a balancing coefficient that controls the weight of the smoothing loss.

IV. EXPERIMENTAL

A. Datasets and Metric

Datasets: The datasets used for training and evaluating our model primarily include TransCG [23], ClearGrasp [21], STD [5]. The ClearGrasp dataset is synthesized using 9 real-world transparent plastic CAD models via the Synthesis AI platform, providing 23,524 samples for training. Its test set includes both synthetic and real-world transparent objects, covering seen and unseen shapes relative to the training set. TransCG offers 57,715 RGB-D images collected by a robotic system in real-world settings. It focuses on 51 everyday objects prone to causing depth sensing errors, such as reflective, transparent, translucent objects, and items with dense holes. STD dataset is a real-world dataset primarily consisting of specular, transparent, and diffuse objects. It is divided into two parts: known(STD-CatKnown) and novel categories(STD-CatNovel), and includes 30 scenes with a total of 27K RGB-D images.

Metrics: We evaluate our depth completion model using 4 widely recognized metrics: RMSE, REL, MAE, and threshold accuracy δ . RMSE quantifies the root mean

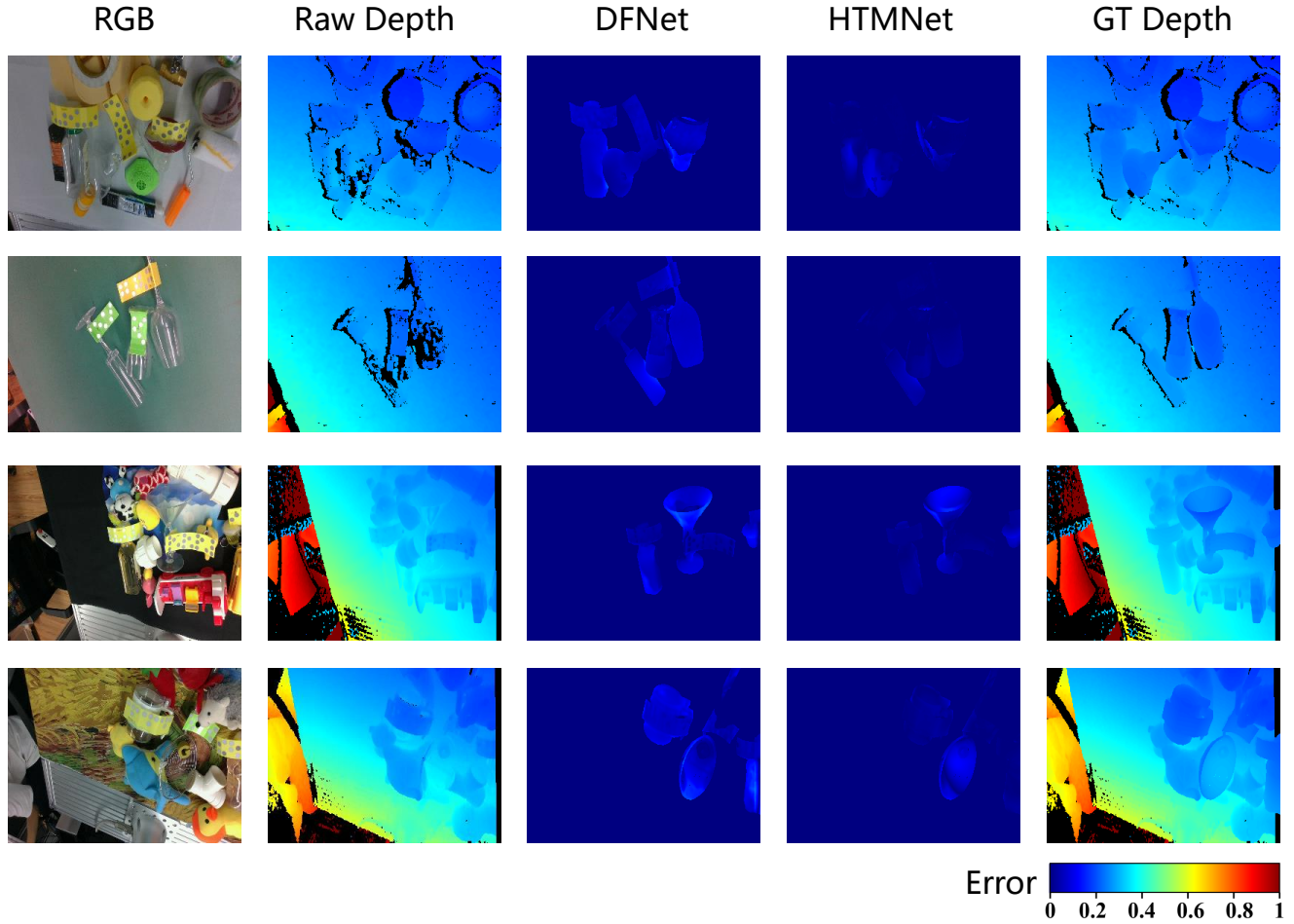


Fig. 7. Depth Completion Visualizations of Different Models on the TransCG Dataset

squared difference, while REL measures the mean absolute relative difference between predictions and ground-truth depths. MAE computes the mean absolute deviation. Threshold accuracy δ indicates the proportion of pixels satisfying $\max\left(\frac{d}{d^*}, \frac{d^*}{d}\right) < \delta$, where d and d^* represent the predicted and ground-truth depths, respectively. In our experiments, δ thresholds are set to 1.05, 1.10, and 1.25.

B. Implementation Details

The experiments were conducted on a system equipped with an Intel Xeon 8358P CPU and an Nvidia RTX 4090 GPU. We employed the AdamW optimizer with an initial learning rate of 0.001 to train the model for 40 epochs, using a batch size of 8. Input images were resized to 320×240 pixels before being processed by the model.

C. Results and Analysis

1) *TransCG Datasets*: We train our model on the TransCG training set and evaluate it on the corresponding test set. As shown in Tab.I, our method achieves

state-of-the-art performance on this dataset. Additionally, we visualize the prediction errors of different methods in Fig.7, focusing exclusively on the transparent regions. The error map is computed as $\frac{|d-d^*|}{d^*}$, where d and d^* denote the predicted depth and the ground truth, respectively. It can be observed that our model produces the most detailed and accurate depth estimations, further demonstrating the effectiveness and superiority of our approach.

TABLE I
PERFORMANCE COMPARISON OF DIFFERENT METHODS ON
TRANSCG DATASET

Methods	RMSE ↓	REL ↓	MAE ↓	$\delta_{1.05} \uparrow$	$\delta_{1.10} \uparrow$	$\delta_{1.25} \uparrow$
CG [21]	0.054	0.083	0.037	50.48	68.68	95.28
DFNet [23]	0.018	0.027	0.012	83.76	95.67	99.71
LIDF [44]	0.019	0.034	0.015	78.22	94.26	99.80
TCRNet [25]	0.017	0.020	0.010	88.96	96.94	99.87
TranspareNet [45]	0.026	0.023	0.013	88.45	96.25	99.42
FDCT [26]	0.015	0.022	0.010	88.18	97.15	99.81
TODE-Trans [24]	0.013	0.019	0.008	90.43	97.39	99.81
DualTransNet [46]	0.012	0.018	0.008	92.37	97.98	99.81
TDCNet [40]	0.012	0.017	0.008	92.25	97.86	99.84
HTMNet (ours)	0.012	0.018	0.008	92.40	98.17	99.87

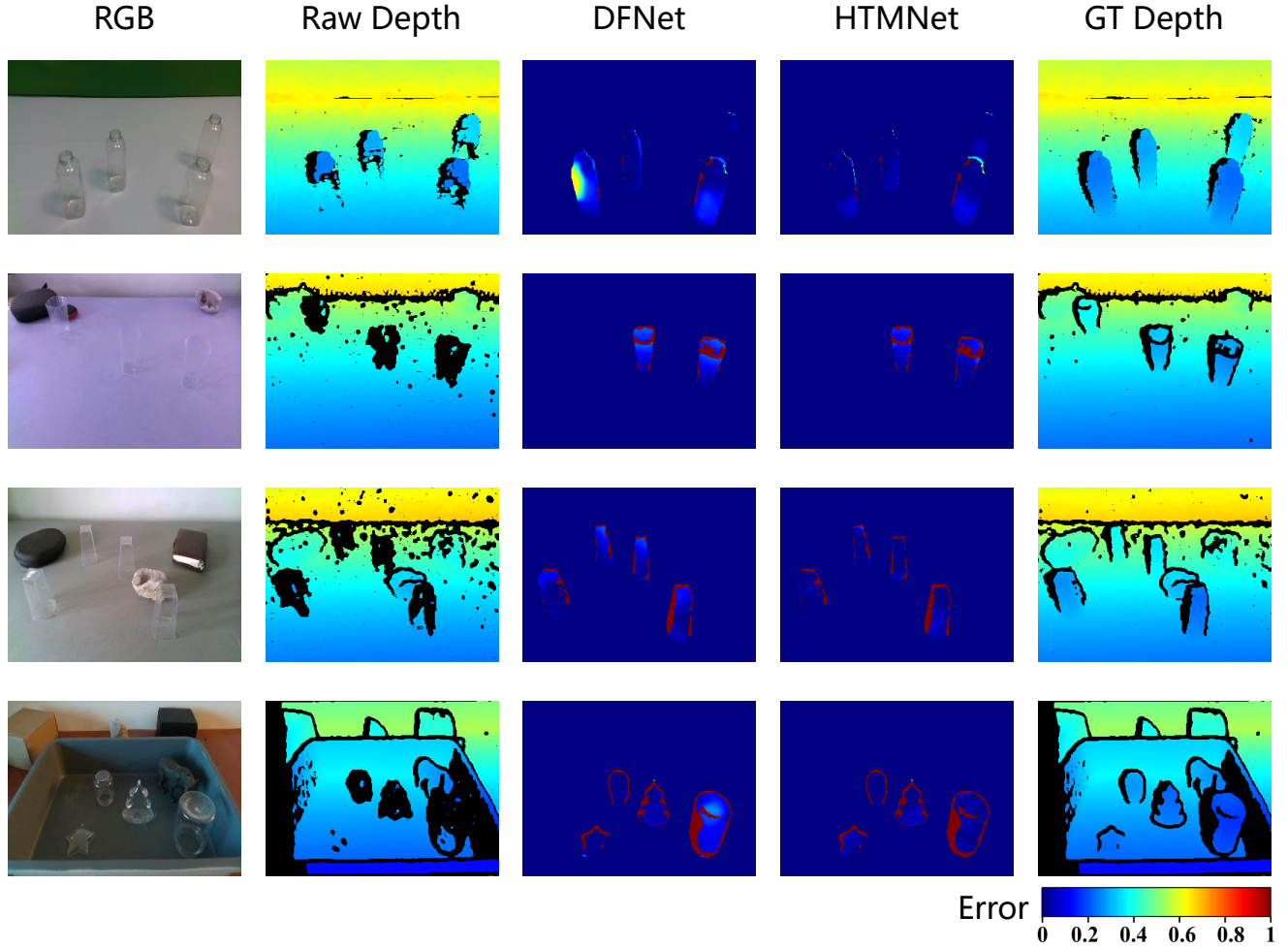


Fig. 8. Depth Completion Visualizations of Different Models on the ClearGrasp Real-world Dataset

2) *Cleargrasp Datasets*: We train our model on ClearGrasp training sets and evaluate it on the ClearGrasp real-world test and val set. The experimental results are shown in Tab.II. The CG [21] results are derived from the evaluation of its publicly available pre-trained model, while the results of DFNet [23], TDCNet [40], and FDCT [26] are obtained by retraining with the official open-source code and hyperparameters. The DITR results are taken from the official paper. The experimental results demonstrate that our method surpasses many existing state-of-the-art approaches and achieves superior performance. Furthermore, we visualize the prediction error in Fig.8. The comparison of metrics and the visualization of depth completion results clearly demonstrate the superiority of our method.

3) *STD Datasets*: We train our model on the STD-CatKnown training set and evaluate it on the test sets of both STD-CatKnown and STD-CatNovel. The experimental results are presented in the Tab.III. For a fair comparison, we retrain other state-of-the-art methods listed in the table using the same training data. We also

TABLE II
COMPARISON OF DIFFERENT METHODS ON REAL-WORLD
CLEARGRASP DATASET.

Method	RMSE	REL	MAE	$\delta_{1.05}$	$\delta_{1.10}$	$\delta_{1.25}$
CG [21]	0.037	0.049	0.027	74.30	88.47	96.27
DFNet [23]	0.026	0.037	0.020	76.69	92.26	99.09
FDCT [26]	0.028	0.038	0.021	76.45	93.36	98.95
TDCNet [40]	0.022	0.031	0.017	82.26	95.83	99.85
DITR [2]	0.019	0.030	0.012	85.11	94.20	98.92
HTMNet(ours)	0.020	0.026	0.015	86.32	96.32	99.67

visualize the prediction results of different methods on the STD dataset, as shown in Fig.9. Both the quantitative results and qualitative visualizations demonstrate the superiority of our proposed method.

D. Limits and Discussion

Although our method achieves state-of-the-art performance in depth completion for transparent and reflective objects, it still exhibits certain limitations. Specifically, by prioritizing the completion accuracy of transparent and reflective regions through reduced training

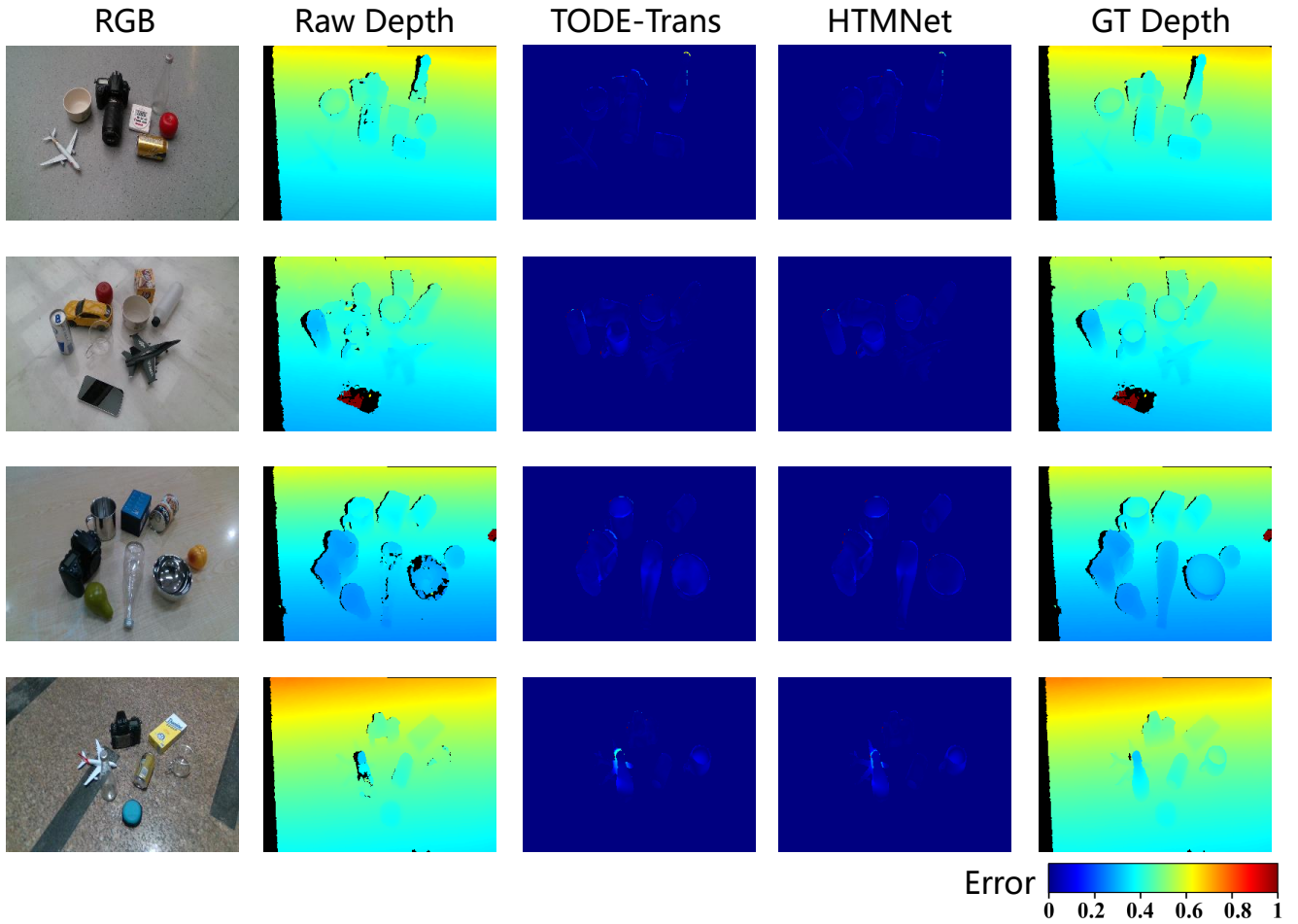


Fig. 9. Depth Completion Visualizations of Different Models on the STDS Real-world Dataset

TABLE III

COMPARISON OF DIFFERENT METHODS ON REAL-WORLD STD DATASET.

Method	RMSE	REL	MAE	$\delta_{1.05}$	$\delta_{1.10}$	$\delta_{1.25}$
DFNet [23]	0.025	0.026	0.016	87.60	95.92	99.05
FDCT [26]	0.024	0.026	0.015	88.17	96.68	99.35
TODE-Trans [24]	0.021	0.022	0.013	90.31	97.39	99.69
HTMNet(ours)	0.019	0.021	0.013	91.26	97.53	99.72

loss weights for non-transparent and non-reflective areas, there exists an inevitable degradation in depth precision for other regions. As illustrated in the Fig.10, while the original depth values of diffuse objects remain accurate, such compromised depth integrity during practical applications could adversely affect downstream tasks like robotic grasping by reducing success rates. This issue, however, remains a common limitation prevalent in existing methods. A potential solution involves incorporating diffuse objects into the loss computation paradigm, as exemplified by the training methodology implemented in the STD dataset, which jointly optimizes depth estimation and classification.

tion for three distinct categories: transparent, reflective, and diffuse objects. As illustrated in Fig.10, the STD dataset is trained on objects spanning all categories present on the desktop surface. This approach ensures reasonable depth accuracy for opaque and non-reflective objects while effectively recovering missing depth information for transparent and reflective objects. Compared to model predictions derived from the TransCG and ClearGrasp datasets, the depth maps generated by the STD dataset exhibit significantly closer alignment with the ground-truth (GT) depth images.

V. ABLATION STUDY

A. Layer-wise Fusion vs. Bottleneck Fusion

To evaluate the advantages of the proposed bottleneck fusion(BF) strategy, we design a layer-wise fusion(LWF) structure as a baseline, where the multimodal fusion module is applied at each stage of the encoder. As shown in Tab.IV, experimental results indicate that fusion at the bottleneck yields marginally superior overall performance compared to layer-wise fusion, along with improved inference throughput.

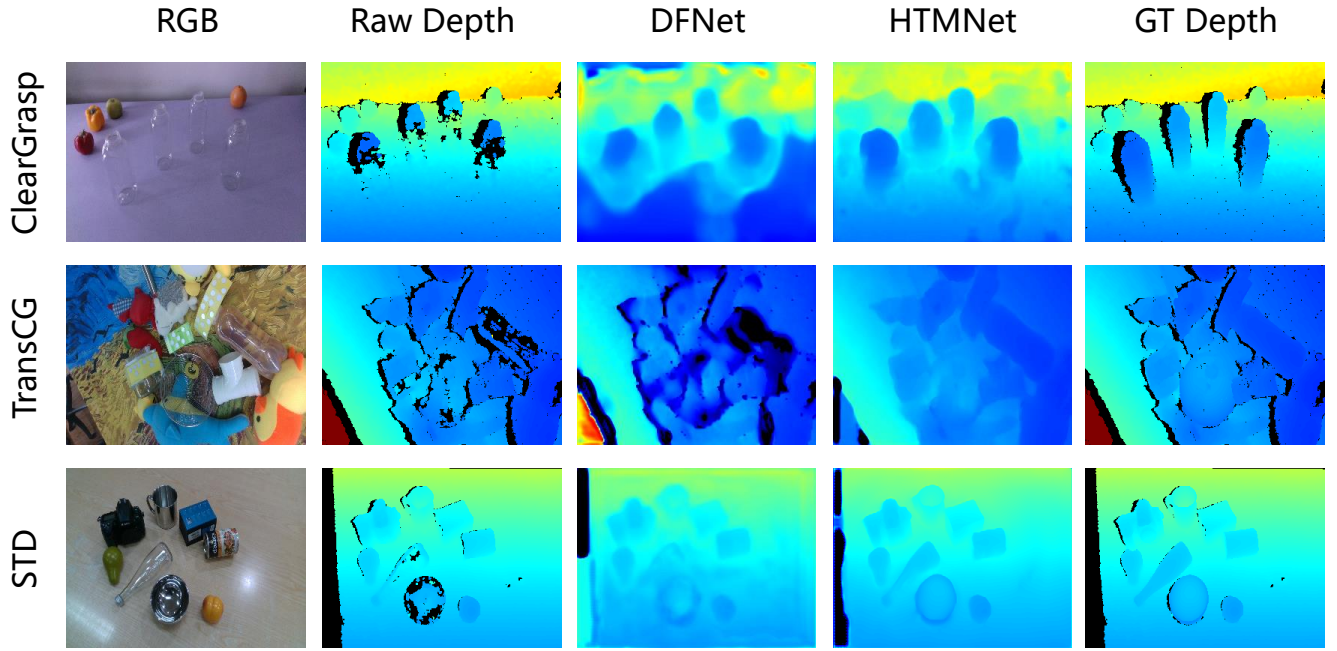


Fig. 10. Depth Completion Visualizations on the Different Real-world Dataset

TABLE IV

PERFORMANCE COMPARISON OF DIFFERENT FUSION METHODS ON TRANS CG DATASET

Model	RMSE ↓	REL ↓	MAE ↓	$\delta_{1.05} \uparrow$	$\delta_{1.10} \uparrow$	$\delta_{1.25} \uparrow$	Param(M)	Throughput(Img/Sec)
LWF	0.012	0.018	0.008	92.51	97.94	99.85	8.57	230
BF	0.012	0.018	0.008	92.40	98.17	99.87	11.31	286

B. Number of Bottleneck Fusion Modules

To investigate the impact of the number of TransMamba modules at the bottleneck on model performance, we conducted a series of ablation studies. As shown in Tab.V, experimental results show that the best performance is achieved when the number of modules is set to 4.

TABLE V

PERFORMANCE COMPARISON OF DIFFERENT NUMBER OF BOTTLENECK FUSION MODULES ON TRANS CG DATASET

Num.	RMSE ↓	REL ↓	MAE ↓	$\delta_{1.05} \uparrow$	$\delta_{1.10} \uparrow$	$\delta_{1.25} \uparrow$
2	0.012	0.018	0.008	92.21	97.85	99.89
4	0.012	0.018	0.008	92.40	98.17	99.87
6	0.012	0.018	0.008	92.34	98.04	99.89

C. The Role of Each Module

We conducted controlled experiments on different modules, as shown in Tab.VI. It can be observed from the table that both the multi-scale fusion module and the bottleneck fusion module contribute to improving the depth completion performance of the model.

TABLE VI

THE ROLE OF DIFFERENT MODULES ON TRANS CG DATASET

MSFM	BFM	RMSE ↓	REL ↓	MAE ↓	$\delta_{1.05} \uparrow$	$\delta_{1.10} \uparrow$	$\delta_{1.25} \uparrow$
		0.013	0.018	0.008	91.82	97.74	99.86
✓		0.012	0.018	0.008	92.35	98.14	99.89
✓	✓	0.012	0.018	0.008	92.40	98.17	99.87

VI. CONCLUSIONS

In this work, we propose a hybrid model named HTM-Net for depth completion of transparent objects. HTM-Net combines multiple architectures, including Transformer, CNN, and Mamba, to enhance model performance. We design a multimodal bottleneck fusion module based on self-attention and state space models, as well as a novel multi-scale fusion module specifically for multi-scale fusion in the decoder. We evaluate our method on several public datasets, achieving state-of-the-art performance. Both quantitative evaluations and visualization results demonstrate the effectiveness of our approach. In the future, we aim to further promote the application of transparent object depth completion in other domains, such as robotic grasping and pose estimation.

REFERENCES

- [1] Z. Cui, H. Sheng, D. Yang, S. Wang, R. Chen, and W. Ke, “Light field depth estimation for non-lambertian objects via adaptive cross operator,” *IEEE Transactions on Circuits and Systems for Video Technology*, vol. 34, no. 2, pp. 1199–1211, 2023.

[2] T. Sun, D. Hu, Y. Dai, and G. Wang, "Diffusion-based depth inpainting for transparent and reflective objects," *IEEE Transactions on Circuits and Systems for Video Technology*, 2024.

[3] H. Wang, K. Zhou, B. Gu, Z. Feng, W. Wang, P. Sun, Y. Xiao, J. Zhang, and H. Dong, "Transdiff: Diffusion-based method for manipulating transparent objects using a single rgb-d image," *arXiv preprint arXiv:2503.12779*, 2025.

[4] Y. Liu, T. Jia, D. Cai, H. Wang, and D. Chen, "Gaa-tso: Geometry-aware assisted depth completion for transparent and specular objects," *arXiv preprint arXiv:2503.17106*, 2025.

[5] Q. Dai, J. Zhang, Q. Li, T. Wu, H. Dong, Z. Liu, P. Tan, and H. Wang, "Domain randomization-enhanced depth simulation and restoration for perceiving and grasping specular and transparent objects," in *European Conference on Computer Vision*. Springer, 2022, pp. 374–391.

[6] Y. Huang, J. Chen, N. Michiels, M. Asim, L. Claesen, and W. Liu, "Distillgrasp: Integrating features correlation with knowledge distillation for depth completion of transparent objects," *IEEE Robotics and Automation Letters*, 2024.

[7] A. Costanzino, P. Z. Ramirez, M. Poggi, F. Tosi, S. Mattoccia, and L. Di Stefano, "Learning depth estimation for transparent and mirror surfaces," in *Proceedings of the IEEE/CVF International Conference on Computer Vision*, 2023, pp. 9244–9255.

[8] Z. Jin, T. Tillo, W. Zou, Y. Zhao, and X. Li, "Robust plane detection using depth information from a consumer depth camera," *IEEE Transactions on Circuits and Systems for Video Technology*, vol. 29, no. 2, pp. 447–460, 2017.

[9] Y. Zhou, W. Peng, Z. Yang, H. Liu, and Y. Sun, "Transparent object depth completion," *arXiv preprint arXiv:2405.15299*, 2024.

[10] Y. Yan, H. Tian, K. Song, Y. Li, Y. Man, and L. Tong, "Transparent object depth perception network for robotic manipulation based on orientation-aware guidance and texture enhancement," *IEEE Transactions on Instrumentation and Measurement*, 2024.

[11] J. Li, T. Sun, Z. Wang, E. Xie, B. Feng, H. Zhang, Z. Yuan, K. Xu, J. Liu, and P. Luo, "Segment, lift and fit: Automatic 3d shape labeling from 2d prompts," in *European Conference on Computer Vision*. Springer, 2024, pp. 407–423.

[12] Q. Shen, Z. Wu, X. Yi, P. Zhou, H. Zhang, S. Yan, and X. Wang, "Gamba: Marry gaussian splatting with mamba for single view 3d reconstruction," *arXiv preprint arXiv:2403.18795*, 2024.

[13] Y. Wang, Y. Mao, Q. Liu, and Y. Dai, "Decomposed guided dynamic filters for efficient rgb-guided depth completion," *IEEE Transactions on Circuits and Systems for Video Technology*, vol. 34, no. 2, pp. 1186–1198, 2023.

[14] Y. Lin, H. Yang, T. Cheng, W. Zhou, and Z. Yin, "Dyspn: Learning dynamic affinity for image-guided depth completion," *IEEE Transactions on Circuits and Systems for Video Technology*, vol. 34, no. 6, pp. 4596–4609, 2023.

[15] D. Chen, T. Huang, Z. Song, S. Deng, and T. Jia, "Aggnet: Attention guided gated-convolutional network for depth image completion," in *Proceedings of the ieee/cvf international conference on computer vision*, 2023, pp. 8853–8862.

[16] H. Wang, M. Wang, Z. Che, Z. Xu, X. Qiao, M. Qi, F. Feng, and J. Tang, "Rgb-depth fusion gan for indoor depth completion," in *Proceedings of the ieee/cvf conference on computer vision and pattern recognition*, 2022, pp. 6209–6218.

[17] R. Rantoson, C. Stolz, D. Fofi, and F. Mériadeau, "3d reconstruction of transparent objects exploiting surface fluorescence caused by uv irradiation," in *2010 IEEE International Conference on Image Processing*. IEEE, 2010, pp. 2965–2968.

[18] B. Wu, Y. Zhou, Y. Qian, M. Gong, and H. Huang, "Full 3d reconstruction of transparent objects," *arXiv preprint arXiv:1805.03482*, 2018.

[19] Y. Zhang and T. Funkhouser, "Deep depth completion of a single rgb-d image," in *Proceedings of the IEEE conference on computer vision and pattern recognition*, 2018, pp. 175–185.

[20] J. Jiang, G. Cao, T.-T. Do, and S. Luo, "A4t: Hierarchical affordance detection for transparent objects depth reconstruction and manipulation," *IEEE Robotics and Automation Letters*, vol. 7, no. 4, pp. 9826–9833, 2022.

[21] S. Sajjan, M. Moore, M. Pan, G. Nagaraja, J. Lee, A. Zeng, and S. Song, "Clear grasp: 3d shape estimation of transparent objects for manipulation," in *2020 IEEE international conference on robotics and automation (ICRA)*. IEEE, 2020, pp. 3634–3642.

[22] Y. Tang, J. Chen, Z. Yang, Z. Lin, Q. Li, and W. Liu, "Depthgrasp: Depth completion of transparent objects using self-attentive adversarial network with spectral residual for grasping," in *2021 IEEE/RSJ International Conference on Intelligent Robots and Systems (IROS)*. IEEE, 2021, pp. 5710–5716.

[23] H. Fang, H.-S. Fang, S. Xu, and C. Lu, "Transcg: A large-scale real-world dataset for transparent object depth completion and a grasping baseline," *IEEE Robotics and Automation Letters*, vol. 7, no. 3, pp. 7383–7390, 2022.

[24] K. Chen, S. Wang, B. Xia, D. Li, Z. Kan, and B. Li, "Tode-trans: Transparent object depth estimation with transformer," in *2023 IEEE international conference on robotics and automation (ICRA)*. IEEE, 2023, pp. 4880–4886.

[25] D.-H. Zhai, S. Yu, W. Wang, Y. Guan, and Y. Xia, "Tcrnet: Transparent object depth completion with cascade refinements," *IEEE Transactions on Automation Science and Engineering*, 2024.

[26] T. Li, Z. Chen, H. Liu, and C. Wang, "Fdct: Fast depth completion for transparent objects," *IEEE Robotics and Automation Letters*, vol. 8, no. 9, pp. 5823–5830, 2023.

[27] A. Dosovitskiy, L. Beyer, A. Kolesnikov, D. Weissenborn, X. Zhai, T. Unterthiner, M. Dehghani, M. Minderer, G. Heigold, S. Gelly *et al.*, "An image is worth 16x16 words: Transformers for image recognition at scale," *arXiv preprint arXiv:2010.11929*, 2020.

[28] Y. Li, K. Zhang, J. Cao, R. Timofte, M. Magno, L. Benini, and L. Van Gool, "Localvit: Analyzing locality in vision transformers," in *2023 IEEE/RSJ International Conference on Intelligent Robots and Systems (IROS)*. IEEE, 2023, pp. 9598–9605.

[29] Z. Peng, W. Huang, S. Gu, L. Xie, Y. Wang, J. Jiao, and Q. Ye, "Conformer: Local features coupling global representations for visual recognition," in *Proceedings of the IEEE/CVF international conference on computer vision*, 2021, pp. 367–376.

[30] Y. Chen, X. Dai, D. Chen, M. Liu, X. Dong, L. Yuan, and Z. Liu, "Mobile-former: Bridging mobilenet and transformer," in *Proceedings of the IEEE/CVF conference on computer vision and pattern recognition*, 2022, pp. 5270–5279.

[31] Y. Wang, Y. Yang, J. Bai, M. Zhang, J. Bai, J. Yu, C. Zhang, G. Huang, and Y. Tong, "Evolving attention with residual convolutions," in *International Conference on Machine Learning*. PMLR, 2021, pp. 10971–10980.

[32] K. Yuan, S. Guo, Z. Liu, A. Zhou, F. Yu, and W. Wu, "Incorporating convolution designs into visual transformers," in *Proceedings of the IEEE/CVF international conference on computer vision*, 2021, pp. 579–588.

[33] Z. Xing, T. Ye, Y. Yang, G. Liu, and L. Zhu, "Segmamba: Long-range sequential modeling mamba for 3d medical image segmentation," in *International Conference on Medical Image Computing and Computer-Assisted Intervention*. Springer, 2024, pp. 578–588.

[34] J. Ma, F. Li, and B. Wang, "U-mamba: Enhancing long-range dependency for biomedical image segmentation," *arXiv preprint arXiv:2401.04722*, 2024.

[35] Y. Liu, Y. Tian, Y. Zhao, H. Yu, L. Xie, Y. Wang, Q. Ye, J. Jiao, and Y. Liu, "Vmamba: Visual state space model," *Advances in neural information processing systems*, vol. 37, pp. 103031–103063, 2024.

[36] A. Hatamizadeh and J. Kautz, "Mambavision: A hybrid mamba-transformer vision backbone," *arXiv preprint arXiv:2407.08083*, 2024.

[37] X. Pei, T. Huang, and C. Xu, "Efficientvmamba: Atrous selective scan for light weight visual mamba," in *Proceedings of the AAAI Conference on Artificial Intelligence*, vol. 39, no. 6, 2025, pp. 6443–6451.

[38] J. Ruan, J. Li, and S. Xiang, "Vm-unet: Vision mamba unet for medical image segmentation," *arXiv preprint arXiv:2402.02491*, 2024.

- [39] Z. Wang, J.-Q. Zheng, Y. Zhang, G. Cui, and L. Li, “Mambunet: Unet-like pure visual mamba for medical image segmentation,” *arXiv preprint arXiv:2402.05079*, 2024.
- [40] X. Fan, C. Ye, A. Deng, X. Wu, M. Pan, and H. Yang, “Tdcnet: Transparent objects depth completion with cnn-transformer dual-branch parallel network,” *arXiv preprint arXiv:2412.14961*, 2024.
- [41] Z. Liu, Y. Lin, Y. Cao, H. Hu, Y. Wei, Z. Zhang, S. Lin, and B. Guo, “Swin transformer: Hierarchical vision transformer using shifted windows,” in *Proceedings of the IEEE/CVF international conference on computer vision*, 2021, pp. 10 012–10 022.
- [42] K. He, X. Zhang, S. Ren, and J. Sun, “Deep residual learning for image recognition,” in *Proceedings of the IEEE conference on computer vision and pattern recognition*, 2016, pp. 770–778.
- [43] Z. Yan, Y. Liu, X. Li, and L. Sun, “Hetero-unet: Heterogeneous transformer with mamba for medical image segmentation,” in *Advancements In Medical Foundation Models: Explainability, Robustness, Security, and Beyond*.
- [44] L. Zhu, A. Mousavian, Y. Xiang, H. Mazhar, J. van Eenbergen, S. Debnath, and D. Fox, “Rgb-d local implicit function for depth completion of transparent objects,” in *Proceedings of the IEEE/CVF Conference on Computer Vision and Pattern Recognition*, 2021, pp. 4649–4658.
- [45] H. Xu, Y. R. Wang, S. Eppel, A. Aspuru-Guzik, F. Shkurti, and A. Garg, “Seeing glass: joint point cloud and depth completion for transparent objects,” *arXiv preprint arXiv:2110.00087*, 2021.
- [46] B. Liu, H. Li, Z. Wang, and T. Xue, “Transparent depth completion using segmentation features,” *ACM Transactions on Multimedia Computing, Communications and Applications*, vol. 20, no. 12, pp. 1–19, 2024.